




Wave beaming and diffraction in quasicrystalline elastic metamaterial plates

Danilo Beli ^{1,*}, Matheus Inguaggiato Nora Rosa ^{2,†}, Carlos De Marqui, Jr. ^{1,‡} and Massimo Ruzzene^{2,§}

¹*Department of Aeronautical Engineering, Sao Carlos School of Engineering, University of Sao Paulo, Sao Carlos-SP 13563-120, Brazil*

²*Department of Mechanical Engineering, College of Engineering and Applied Science, University of Colorado Boulder, Boulder, Colorado 80309, USA*



(Received 31 January 2022; revised 8 August 2022; accepted 25 August 2022; published 17 October 2022)

In this paper, we present evidence of directional wave behavior, i.e., beaming and diffraction, along high-order rotational symmetries of quasicrystalline elastic metamaterial plates. These structures are obtained by placing pillars on an elastic plate following a particular rotational symmetry arrangement, such as eightfold and tenfold rotational symmetries, as enforced by a design procedure in reciprocal space. We estimate the dispersion properties of the waves propagating in the plates through Fourier transformation of transient wave fields. The procedure identifies, both numerically and experimentally, the existence of anisotropic bands characterized by high-energy density at isolated zones in reciprocal space that follow their higher order rotational symmetry. Specific directional behavior is showcased at the identified frequency bands, such as wave beaming (predicted in simulations and confirmed experimentally) and diffraction (exemplified only with numerical results). This paper expands the wave directionality phenomena beyond the symmetries of periodic configurations (e.g., fourfold and sixfold), and opens possibilities for applications involving the unusual high-order wave features of the quasicrystals (e.g., eightfold and tenfold) such as superior guiding, focusing, sensing, and imaging.

DOI: [10.1103/PhysRevResearch.4.043030](https://doi.org/10.1103/PhysRevResearch.4.043030)

I. INTRODUCTION

Periodic configurations have dominated the designs of phononic crystals and metamaterials in past decades. Although the wave features of architected materials are usually associated with their crystalline symmetry and translational periodicity [1–3], nonperiodic configurations have also been explored to achieve various wave manipulation capabilities [4–6]. For example, trivial defects and topological interfaces have been employed for flexible wave guiding [7–9] and, also, spatially correlated unit cells (e.g., rainbow) or disorder have shown the ability to trap waves and broadband vibration attenuation [10,11]. In this context, quasiperiodic phononic configurations or quasicrystals have emerged as relevant candidates for unusual wave phenomena [12]. Their configurations in physical space lack translational periodicity, but long-range order as well as high-order rotational symmetries are present [13]. The unique symmetries of quasicrystals are revealed by their exotic sharp Bragg diffraction patterns, experimentally observed by Shechtman *et al.* [14] and theoretically reported in the pioneering work of Levine and Steinhardt [15]. Investigation of properties arising from

such unique symmetries has resulted in applications such as lasing [16,17], superior sensing and imaging [18], guiding and bending of waves [19], superfocusing [13], superconductivity [20], and topological wave transport [21,22].

In the context of elastic materials, the higher order rotational symmetries of quasicrystals has been shown to induce nearly isotropic stiffness properties in lattice structures [23,24] and continuum elastic composites [25], which results in omnidirectional wave propagation at low frequencies. Their mechanical isotropy can also make them less sensitive to geometric and material variabilities [26]. Similar to the phononic crystals, band gaps or pseudogaps have also been observed in phononic quasicrystals [27]; their bands, however, usually split in several mini bands due to their fractal nature [28]. In addition, the dispersion properties of quasicrystals are associated with their representation in wave number space, which has motivated a pseudo-Brillouin-zone definition [17,29]. The approximated dispersion, however, has been computed only for simple quasiperiodic lattices [30,31] and, in most cases, assuming a periodic approximation. Other works have investigated the wave-guiding capabilities of quasicrystals with [32] or without [33,34] defects. More recently, quasiperiodic arrangements have also been employed to pursue higher dimensional topological features [35], which emanate from the existence of additional parameters (such as the phason) and provide opportunities for topological states with corner localization [36], lower dimension guiding, and pumping [37–39]. Quasiperiodic configurations for such topological phenomena have been obtained by modulation procedures in 1D lattices [40–42] and by the relative twisting of two periodic layers in 2D lattices [43–46].

Despite the recent interest in the dynamics of quasiperiodic systems, their dispersion and wave directionality properties

*dbeli@usp.br, beli.danilo@gmail.com

†matheus.rosa@colorado.edu

‡demarqui@sc.usp.br

§massimo.ruzzene@colorado.edu

are still largely unexplored or scarce. Indeed, wave directionality finds applications that involve wave filtering and guiding, ultrasonic therapy and imaging, antennas, sensors and lenses; however, the wave fronts are currently restricted to known crystallographic symmetries (e.g., bilayer, square and hexagonal) [47,48]. The elastic wave directivity was initially investigated in periodic lattice structures [49,50], and later in periodic continuum structures with Bragg band gaps [51] and locally resonant gaps [52,53]. As we illustrate herein, quasiperiodic configurations expand the wave directionality and beaming possibilities beyond the symmetries of periodic arrangements. Inspired by previous work on quasicrystalline composites [25], we investigate the spectral properties, with a particular focus on their directional wave behavior, of elastic plates whose higher order rotational symmetries are enforced through a design procedure in reciprocal space. The dispersion properties of the quasicrystalline plates (i.e., eight- and tenfold) are estimated from transient wave fields and their 3D Fourier transforms. The procedure identifies anisotropic frequency bands where directional wave behavior is observed, in particular, wave beaming (numerically and experimentally) and diffraction (numerically). The results of this paper highlight unexplored features of the wave behavior in quasicrystalline media, i.e., directionality in high-order rotational symmetries, and open possibilities for practical implementations in structural components and wave devices.

This paper is organized as follows: Following this introduction, Sec. II describes the design of the quasicrystalline plates, along with the experimental setup and numerical modeling. Next, Sec. III describes the dispersion properties, followed by the wave-beaming phenomena in Sec. IV, and diffraction in Sec. V. Section VI summarizes the main contributions of this paper and outlines possible future directions.

II. QUASICRYSTALLINE PLATES

The design of the quasiperiodic elastic metamaterial plates is based on the geometric representation in 2D wave-number space [25,54,55]. A continuum distribution in physical space $\phi(\mathbf{r})$, with $\mathbf{r} = [x, y] \in \mathcal{R}^2$, is defined by directly assigning N Bragg peaks in reciprocal space ($\mathbf{k} = [k_x, k_y] \in \mathcal{R}^2$) as points in the two-dimensional Fourier spectra [13]. These Bragg peaks are angularly spaced by $\theta_N = 2\pi/N$ over a circle of fundamental wave number k_0 . In this paper, only an even number of peaks is considered to guarantee a real distribution in physical space. Therefore, reciprocal and physical spaces can be expressed, respectively, as

$$\hat{\phi}(\mathbf{k}) = \sum_{n=0}^{N-1} \delta(\mathbf{k} - \mathbf{k}_n) \quad \text{and} \quad \phi(\mathbf{r}) = \sum_{n=0}^{N-1} e^{i\mathbf{k}_n \cdot \mathbf{r}}, \quad (1)$$

where δ is the delta function that locates the wave number \mathbf{k}_n of each Bragg peak; moreover, $\mathbf{k}_n = k_0[\cos(n\theta_N), \sin(n\theta_N)]$, with $n = 0, \dots, N-1$ and $k_0 = 2\pi/\lambda_0$ is the radius of the design circle in reciprocal space, where λ_0 is the fundamental wavelength. In this design strategy, a single parameter N defines the rotational symmetry of the distribution in physical space, which leads to periodic (i.e., crystalline) distributions

(1D bilayer for $N = 2$, square pattern for $N = 4$ and hexagonal pattern for $N = 6$) or quasiperiodic (i.e., quasicrystalline) distributions with rotationally N -fold symmetry such as the eightfold and tenfold.

For practical implementations in elastic continuum structures, a two-phase distribution is desirable and, hence, a threshold procedure is applied to the real continuum field. This distribution $\bar{\phi}(\mathbf{r})$ assumes only two phases, which are produced by comparing the local field level to a chosen level $\bar{\phi}_0$: Phase A is defined for $\phi(\mathbf{r}) \leq \bar{\phi}_0$ and phase B is defined for $\phi(\mathbf{r}) > \bar{\phi}_0$. Based on the phase ratio, a volume (or filling) fraction is defined by $\text{vf} = v_B/(v_A + v_B)$. Herein, the metamaterial plates are designed by using a single material with geometric thickness modulation given by $\bar{\phi}(\mathbf{r})$, where a flat plate (phase A) is partially covered on one side by pillars (phase B). These geometries can be conveniently manufactured using regular additive manufacturing technologies. Moreover, experimental observations can be performed through vibration measurements on the flat side. Figure 1 summarizes the design process, from the choice of Bragg peaks in the reciprocal space to the three-dimensional printed plate with ten- and eightfold symmetries and $\text{vf} = 0.30$ (please check the Appendix for the four- and sixfold metamaterial plates). Reference [25] details this design strategy for other fold symmetries and volume fractions considering 2D domains with material phase modulation and in-plane wave behavior, i.e., Figs. 1(a) and 1(b).

The plates have a square domain in the xy plane of size $L = 0.2$ m and $\lambda_0 = 5$ mm, and their modulated thickness in the z axis is given by $h(\mathbf{r}) = h_A + \bar{\phi}(\mathbf{r})(h_B - h_A)$, where $h_A = 4$ mm and $h_B = 12$ mm. In addition, they are manufactured using a selective laser sintering process (in a Stratasys machine with geometric refinement of $0.1 \times 0.1 \times 0.2$ mm) and polymer nylon 12 material, with nominal elastic properties: Mass density $\rho_n = 1500$ kg/m³, elastic modulus $E_n = 5$ GPa, and Poisson ratio $\nu_n = 0.3$.

Experimental setup and numerical modeling

The experimental setup is shown in Fig. 2, where free boundary conditions are emulated by suspending the plate by nylon strings. The input excitation is due to a circular piezoelectric transducer placed at the center of the flat side. In this paper, only the flexural behavior (i.e., bending waves) is considered, and the out-of-plane velocities of a rectangular grid composed of 315×315 points on the flat side of the plate are measured by a scanning laser Doppler vibrometer connected to a data acquisition and signal processing unit that stores the experimental results.

The numerical simulations are conducted using the finite element (FE) approach within the COMSOL MULTIPHYSICS environment, where 3D elastic solid elements with linear strains are employed. The FE discretization results in equations of the form $\mathbf{M}\ddot{\mathbf{u}}(\mathbf{r}, t) + \mathbf{K}\mathbf{u}(\mathbf{r}, t) = \mathbf{f}(\mathbf{r}, t)$, where \mathbf{M} is the mass matrix, \mathbf{K} is the stiffness matrix, \mathbf{u} is the displacement vector, and \mathbf{f} is the externally applied load vector. The employed meshes comprise ten elements per wavelength, i.e., $\Delta a = \lambda_0/10$, and for time response simulations, a time step of $\Delta t = 1/(20f_e)$ is used to appropriately describe the dynamic behavior, where f_e is the excitation frequency in Hz.

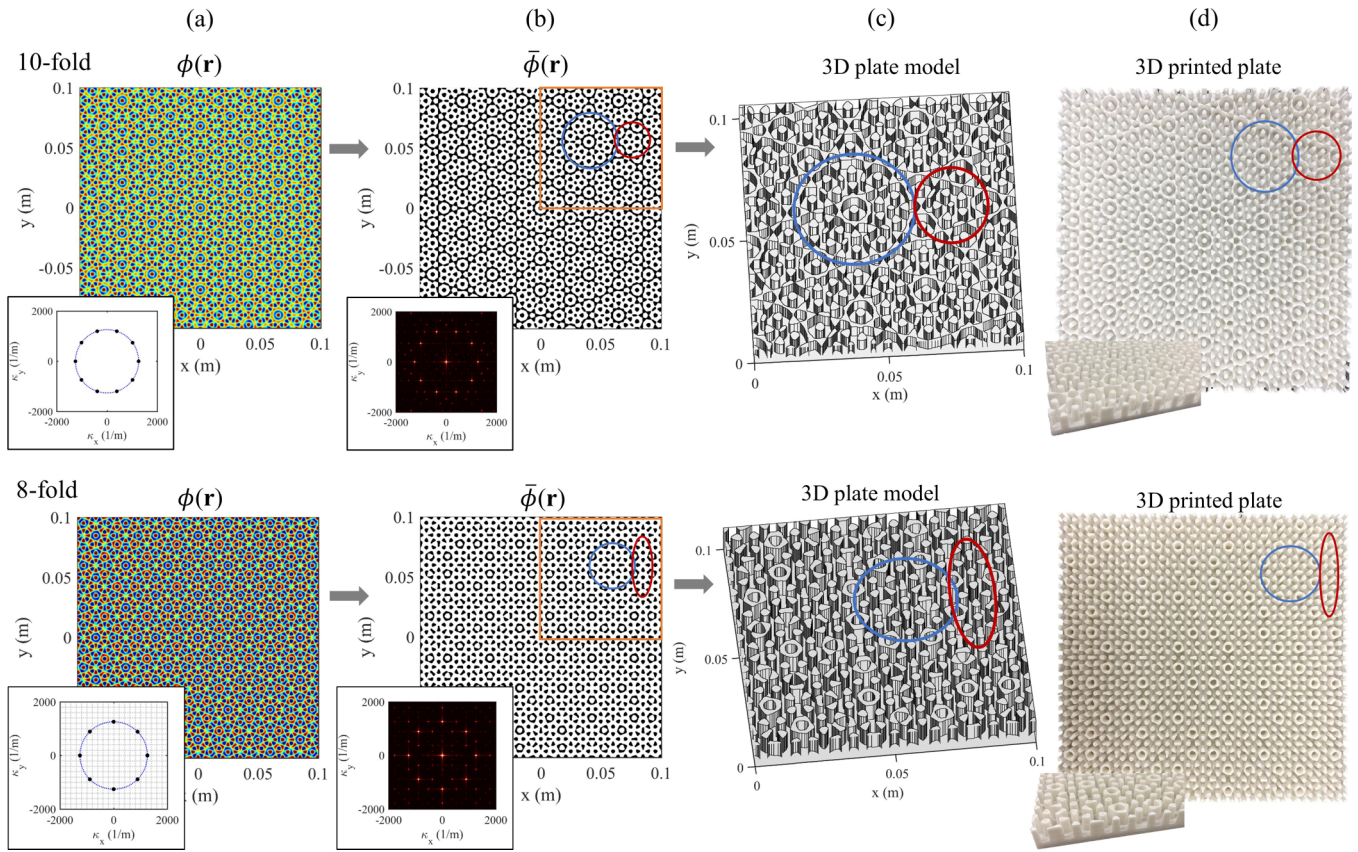


FIG. 1. Design strategy for the ten- (top row) and eightfold (bottom row) symmetries with $\nu f = 0.30$: Two-dimensional physical distribution by assigning, respectively, ten and eight Bragg peaks (a), two-phase distribution after applying the threshold procedure and its Fourier transform (i.e., diffraction pattern) (b): Phase A (white) and phase B (black). Three-dimensional quasiperiodic plate obtained by extruding phase B toward z direction, which produces the geometry in (c) and the correspondent 3D printed quasiperiodic plate (d).

III. DISPERSION CHARACTERIZATION

Dispersion properties are used to understand and predict the dynamic behavior of phononic and metamaterial structures related to wave propagation and manipulation. For crystalline (i.e., periodic) materials, the band structure is obtained by enforcing Bloch conditions on the unit-cell boundaries. How-

ever, Bloch-Floquet theory cannot be applied to the present quasicrystalline plates due to their lack of translational periodicity. Instead, we rely on transient wave fields $\mathbf{u}(x, y, t)$, and their correspondent 3D-FT (Fourier transform), $\hat{\mathbf{U}}(k_x, k_y, \omega)$, to estimate the dispersion properties of the quasicrystalline plates.

In both simulations and experiments, time transient analyses with sinusoidal burst excitation signals are performed with 1-2 cycles for a center frequency of 25 kHz to characterize the dispersion in a broad frequency band of interest. Next, 3D-FTs are performed on the displacement fields $\mathbf{u}(x, y, t)$, providing a representation in reciprocal space where each coordinate (k_x, k_y, ω) has a wave amplitude $\hat{\mathbf{U}}(k_x, k_y, \omega)$. To reduce effects of unwanted noise at low amplitudes and to improve visualization, the dispersion results are filtered such that only points in the spectrum with higher wave amplitudes are plotted (higher than 0.80 and 0.70 of the maximum value in each frequency for numerical and experimental results, respectively). This approach is validated based on the periodic cases (i.e., four- and sixfold plates), whose bands and band gaps are readily available from the application of Bloch analysis, which leads to the eigenvalue problem $\omega(\kappa)$,

$$[\hat{\mathbf{K}}(\kappa) - \omega^2(\kappa)\hat{\mathbf{M}}(\kappa)]\mathbf{u}(\kappa) = 0, \quad (2)$$

where κ is the wave vector, $\hat{\mathbf{K}}(\kappa)$ and $\hat{\mathbf{M}}(\kappa)$ are the stiffness and mass FE matrices of the unit cell after applying

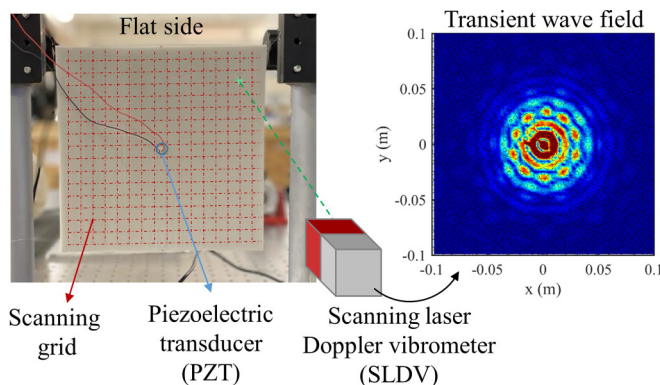


FIG. 2. Experimental setup for time-response observations, the PZT transducer excitation, and the SLDV measurements are placed on the flat side of the plate, which recovers the two-dimensional wave field for each instant of time.

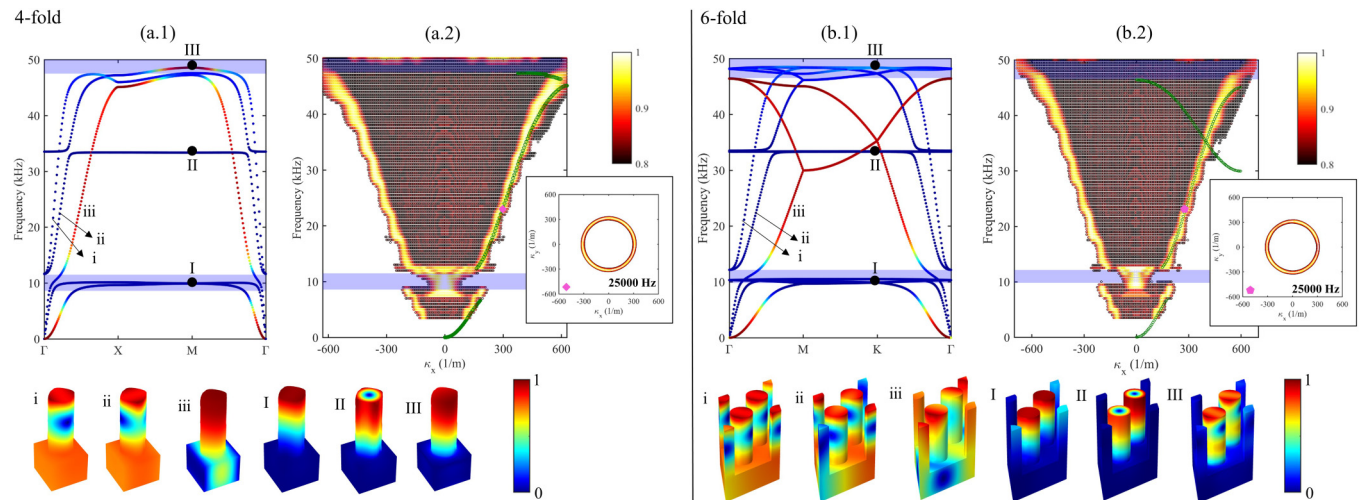


FIG. 3. Band structure (a.1), (b.1) computed by applying Bloch-Floquet conditions at fourfold and sixfold unit cell boundaries. The colors represent the wave polarizations: In plane (blue) and out of plane (red). The wave mode shapes at each locally resonant band gap are also presented; their colors represent the displacement amplitudes: Low (blue) and high (red). The approximate band structure obtained from the time response simulation and its Fourier transform (a.2), (b.2) are compared to the dispersion computed by Bloch-Floquet theory (green) at ΓX and ΓK directions, respectively.

the Bloch periodicity conditions [2]. For the band-structure computation, κ is swept over the correspondent first Brillouin zone contour. The bending waves, which have mainly out-of-plane motion, are distinguished by the wave polarization computation given by $p_z = [\int u_z^2 dV] / [\int (u_x^2 + u_y^2 + u_z^2) dV]$, where u_i is the displacement of the wave-mode shape at the direction $i \in [x, y, z]$. The polarization p_z is linked to the bending wave and ranges from 0 (pure in-plane motion) to 1 (pure out-of-plane motion). The dispersion computation of the periodic plates is also used to guide the dispersion analysis in the quasicrystalline plates.

The dispersion results computed via Bloch-Floquet theory are presented in Figs. 3(a.1) and 3(b.1) for the fourfold and sixfold plates (please check their designs in the Appendix). Three main waves are distinguished: Longitudinal (i), shear (ii), and flexural (iii), as pointed out by the wave-mode shapes. Three band gaps related to the pillars resonances are opened: The first around 10 kHz is related to the flexural motion of the pillars (I), the second around 35 kHz is related to torsional motion coupling only to the shear wave (II), and the third around 50 kHz is related to the second flexural mode and opens a full band gap (III). The approximate dispersion surfaces computed by the time response and the 3D-FT are shown in Figs. 3(a.2) and 3(b.2). A good agreement with the exact dispersion Figs. 3(a.1) and 3(b.1) is observed in the propagating bands and band gaps for the bending wave. For both periodic plates, the numerical and experimental approximate dispersion surfaces present circular wave-number contours [insets in Figs. 3(a.2) and 3(b.2)] for almost every frequency in the spectrum, revealing an isotropic dispersion (please see the Appendix for a more complete dispersion characterization of the periodic cases).

Following this validation, the dispersion behavior of the quasicrystalline plates is first exemplified by the tenfold case (i.e., $N = 10$), whose design is illustrated in Fig. 1, and with results summarized in Fig. 4. Overall, a good agreement between numerical simulations and experimental observations

has been achieved despite a frequency shift of roughly 5 kHz, which we attribute to uncertainties in the properties of the 3D printed material. The dispersion surfaces for the flexural waves are characterized by a tenfold rotational symmetry that manifests throughout the majority of the bands, as highlighted by the contours displayed for selected frequencies. In particular, several bands of highly anisotropic contours are identified, which are characterized by ten separated peaks of high amplitude in reciprocal space forming the tenfold symmetry. We note that the rotational symmetry twists by $\theta_N/2 = 18^\circ$ in certain frequency ranges shown in Fig. 4(b), for example, around 22, 26, and 35 kHz. One transition example is highlighted by the selected contours of Fig. 4(c), changing from a given tenfold symmetry arrangement (pink marker) to an almost circular contour (green marker) and then to another tenfold symmetric arrangement (blue marker), but twisted by $\theta_N/2 = 18^\circ$ with respect to the previous case (pink marker). This behavior is confirmed by the experimental results of Figs. 4(e) and 4(f), and highlights how the dispersion properties of the quasicrystalline plates are characterized by several bands that preserve the N -fold symmetry of the design and may present different anisotropy directions.

The dispersion behavior for the eightfold elastic metamaterial plate, whose design is presented in Fig. 1, is shown in Fig. 5, where numerical and experimental results are also in a good agreement despite a frequency shift of 2 kHz. The dispersion surfaces for the bending waves have an eightfold rotational symmetry that appear especially above 20 kHz, as highlighted by the contours displayed for selected frequencies. The contours are characterized by eight peaks (traces) of high amplitude in reciprocal space shaping the eightfold symmetry. Similar to the tenfold case, the eightfold dispersion has a rotational symmetry twist by $\theta_N/2 = 22.5^\circ$ in certain frequency ranges (i.e., the peaks (traces) change the orientation) as shown in Fig. 5(b), for example, around 39 kHz. This transition is highlighted by the selected contours of Fig. 5(c), changing from a given eightfold symmetry arrange-

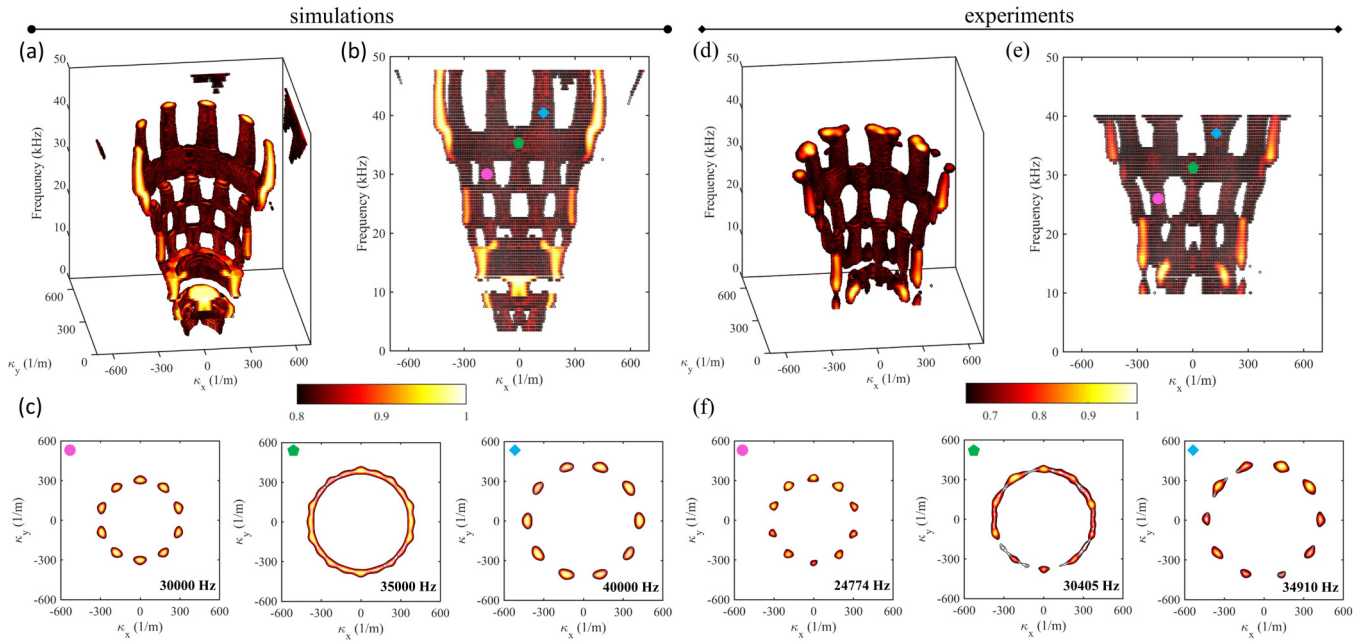


FIG. 4. Dispersion properties of the tenfold quasicrystal plate obtained by numerical simulations (a)–(c) and experiments (d)–(f). Approximated dispersion surfaces obtained by 3D Fourier transform of the time response: 3D view (a), (d) and sectional view on $\kappa_x\omega$ plane (b), (e). Contours at specific frequencies showing the transition between two bands twisted by $\theta_N/2$ (c), (f).

ment (pink marker), to an almost circular contour (green marker), and then to another eightfold symmetric arrangement (blue marker), but twisted by $\theta_N/2 = 22.5^\circ$ with respect to the previous case (pink marker). This behavior is also captured by the experimental results of Figs. 5(e) and 5(f). Therefore, the eightfold metamaterial plate also presents several bands following the quasicrystal symmetry that may have differ-

ent anisotropic orientations; however, for the same frequency range, it presents a smaller number of anisotropic bands when compared to the tenfold case.

In summary, the quasicrystalline plates (ten- and eightfold) present zones of high anisotropy characterized by $N = 10$ or $N = 8$ peaks of high amplitude in reciprocal space that follows their rotational symmetry. The periodic (or crystalline)

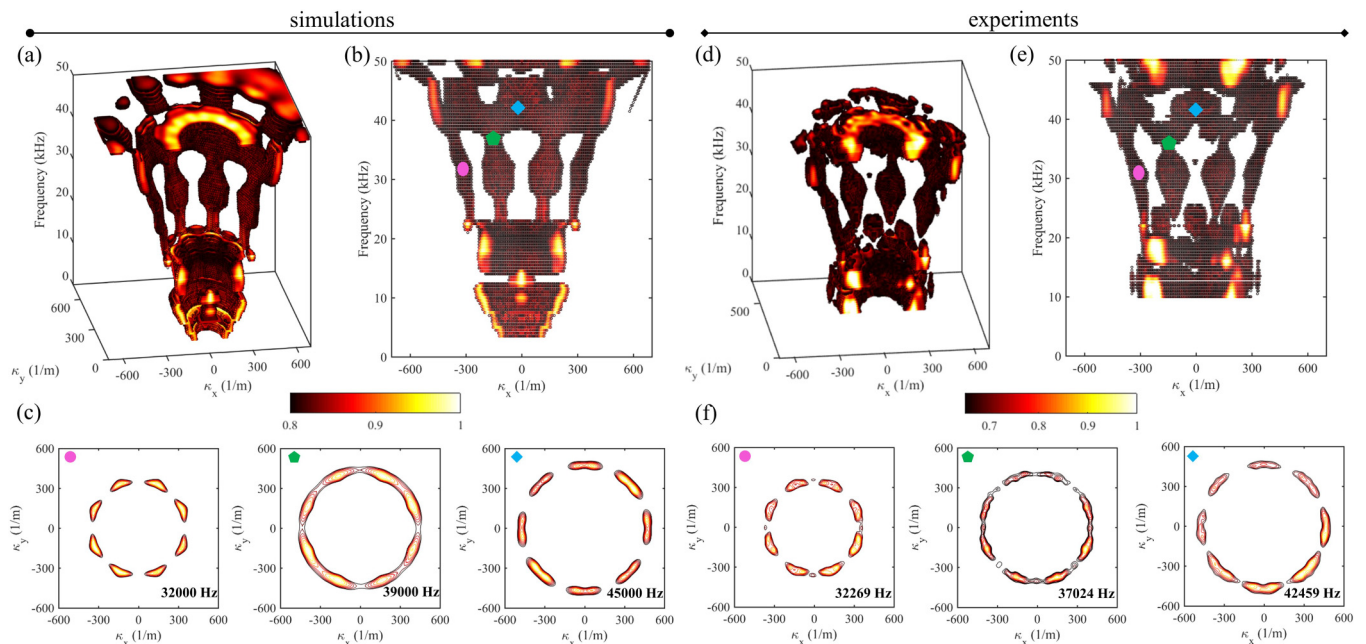


FIG. 5. Dispersion properties of the eightfold quasicrystal plate obtained by numerical simulations (a)–(c) and experiments (d)–(f). Approximated dispersion surfaces obtained by 3D Fourier transform of the time response: 3D view (a), (d) and sectional view on $\kappa_x\omega$ plane (b), (e). Contours at specific frequencies showing the transition between two bands twisted by $\theta_N/2$ (c), (f).

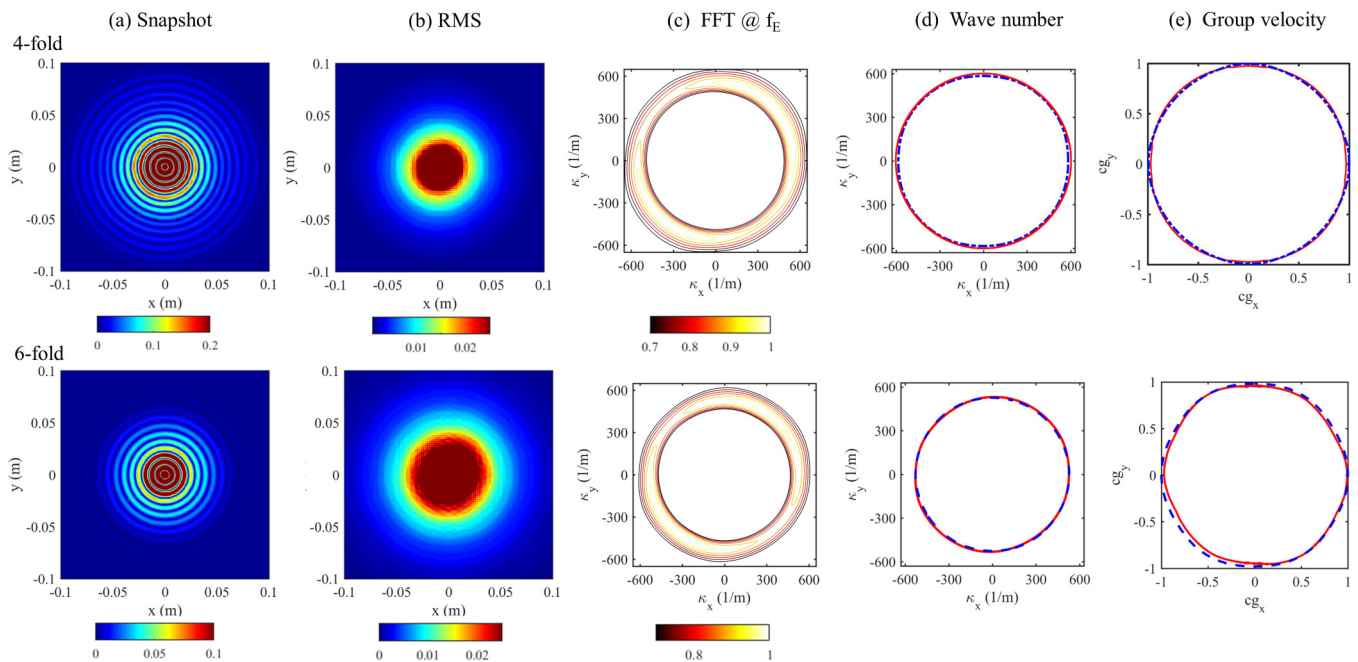


FIG. 6. Wave-propagation analysis at 45 kHz for the fourfold (top) and sixfold (bottom) metamaterial plate. Snapshot (a) and RMS of the displacement field over time (b) and the wave-number contour at the excitation frequency obtained by the 3D-FT (c). The wave-number contour (d) and the correspondent normalized group velocity pattern (e): Approximate results obtained by the approach presented in Eq. (4) and the results computed by using the Bloch-Floquet theory (red line).

plates (i.e., four- and sixfold), however, exhibit continuous and highly isotropic bands with almost circular contours (please see the Appendix). The periodic plates are characterized by identical pillars repeated periodically in space, therefore they produce only a few and well-defined local-resonant gaps for the flexural wave: One around 10 kHz and another around 48 kHz. On the other hand, the quasicrystalline plates are characterized by numerous different pillars, of different resonance frequencies, which are arranged in space according to their higher order rotational symmetry. Hence, the anisotropic N -fold symmetric bands of the quasicrystalline plates seem to emerge from a combination of multiple local resonances that interact and interfere on a higher-order symmetric pattern. As a result, the continuous bands of the periodic plates are split into several minibands in the quasicrystalline cases, the number of which seems to increase with N . This behavior is reminiscent of the fractal nature of spectra in quasiperiodic lattices, usually represented via a Hofstadter butterfly spectrum that ranges from periodic lattices with few continuous bands to quasiperiodic lattices with infinite subbands [40–42,56].

IV. WAVE DIRECTIONALITY

Next, we illustrate in more detail the wave directionality associated with the anisotropic frequency bands identified in the previous section. For such analysis, the transient behavior at selected frequencies is observed by computing the response to narrow-band sinusoidal burst signals (the number of excitation cycles is adjusted for each frequency so the excitation signal ends as the wave reaches the boundaries of the plate). The directional behavior is further elucidated by estimating the group velocity at the excitation frequencies.

For periodic materials, the wave-propagation directions at a given frequency can be characterized by the group velocity, i.e., $\mathbf{c}_g = \nabla_{\kappa} \omega(\kappa)$, where $\omega(\kappa)$ represents the dispersion of the Bloch bands [2]. This implies that the waves propagate along directions normal to the wave number contour at a constant frequency. In the absence of periodicity, we attempt to numerically estimate the group velocities of the quasicrystalline plates based on the dispersion results reported in the previous section. The computation procedure relies on the estimation of the wave number contours for each frequency, their representation in cylindrical coordinates, and a derivative computation through a finite difference approximation. This procedure is validated against traditional computations using the Bloch-Floquet theory for periodic configurations. The wave-number contour is estimated using the approximate dispersion results (3D-FT), and for a direction given by the angle $\alpha \in [0, 2\pi]$, the approximate wave number at the frequency ω_j is given by the weighted average,

$$\kappa_{\alpha}(\omega_j) = \frac{\sum_i \kappa_{ri} [\hat{U}_t(\kappa_{ri}, \omega_j)]^{\beta}}{\sum_i [\hat{U}_t(\kappa_{ri}, \omega_j)]^{\beta}}, \quad (3)$$

where β is the weighted parameter applied on the normalized Fourier coefficients \hat{U}_t ($\beta = 5$ has been used in this paper), and $\kappa_{ri} = (\kappa_{xi}^2 + \kappa_{yi}^2)^{1/2}$ is the radial wave number at the direction α . Therefore, the group velocity for an angular direction α is numerically computed through the finite difference,

$$c_{\alpha}(\omega_j) = \frac{\partial \omega_j}{\partial \kappa_{\alpha}} \approx \frac{\omega_{j+1} - \omega_j}{\kappa_{\alpha}(\omega_{j+1}) - \kappa_{\alpha}(\omega_j)}, \quad (4)$$

with $\omega_{j+1} \rightarrow \omega_j$.

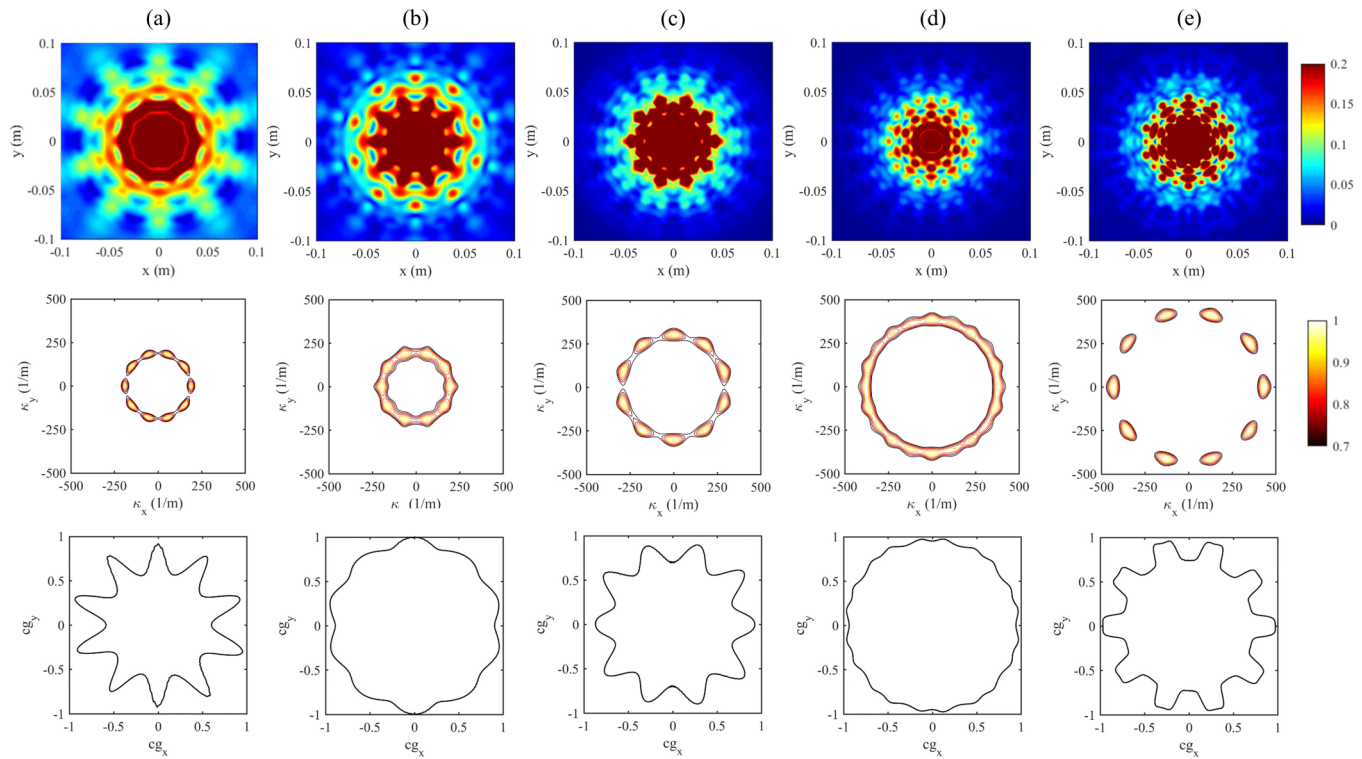


FIG. 7. Directional wave behavior for the tenfold metamaterial plate at different excitation frequencies: 9.3 kHz (a), 15 kHz (b), 30 kHz (c), 35 kHz (d), and 45 kHz (e). The first row corresponds to the RMS of the wave field averaging across all time, the second row corresponds to the RMS of the wave number contours averaging across all frequencies, and the third row corresponds to the estimated group velocity contour at the center frequency

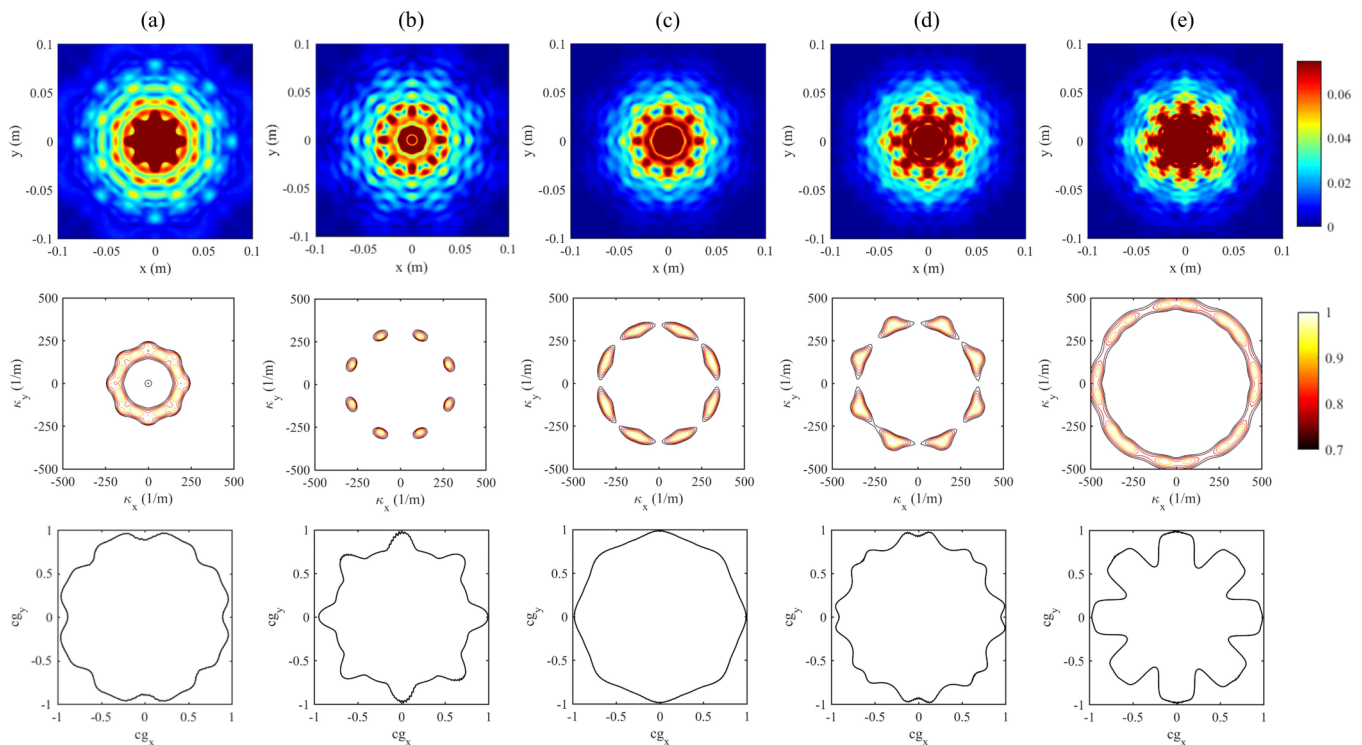


FIG. 8. Directional wave behavior for the eightfold metamaterial plate at different excitation frequencies: 15 kHz (a), 25 kHz (b), 30 kHz (c), 35 kHz (d), and 45 kHz (e). The first row corresponds to the RMS of the wave field averaging across all time, the second row corresponds to the RMS of the wave number contours averaging across all frequencies, and the third row corresponds to the estimated group velocity contour at the center frequency.

The procedure to obtain the group velocity contours is illustrated and validated in Fig. 6 for the fourfold and sixfold configurations. The approximate wave-number contours as well as the group velocity contours obtained from the approximate dispersion surfaces (blue dashed lines) are compared to the contours computed using the Bloch-Floquet theory (red lines). A good agreement between the results is achieved for the selected frequencies. In addition, the group velocity contours are correlated to the rotational symmetry and to the wave propagation patterns depicted in the snapshot and time root mean square (RMS) results. While the fourfold plate exhibits omnidirectional wave propagation at 45 kHz, the sixfold plate presents a slightly anisotropic wave propagation with a hexagonal shape in the group velocity at the same frequency. These results validate the group velocity information obtained through the transient wave-field dispersion data, which we exploit in the following for the quasicrystalline plates.

Figure 7 displays the numerical predictions for the tenfold metamaterial plate. Each column corresponds to a different excitation frequency in the range from 9.3kHz to 45kHz; the panels in the first row display the RMS of the time response, while the second row displays the RMS wave numbers computed by using the 3D-FT of the response. The third row displays the approximate group velocity contours at the excitation frequency, which are in good agreement with the observed wave fields. Specifically, at 9.3kHz [Fig. 7(a)] the waves propagate preferentially along ten symmetric directions in a wave-beaming fashion. The Fourier transform shows ten Fourier peaks that characterize such behavior, while the group velocity further confirms the preferential directions of wave propagation. At the excitation frequency of 15kHz [Fig. 7(b)], a transition between two anisotropic bands [Figs. 7(a) and 7(c)], wave propagation is not strongly directional, as confirmed by the almost circular contour in the reciprocal space, and by the smoother group velocity plot. For 30 kHz [Fig. 7(c)], we observe another directional wave beaming which occurs along directions twisted by $\theta_N/2 = 18^\circ$ with respect to the case in Fig. 7(a). Another transition at the excitation frequency of 35kHz is illustrated in Fig. 7(d), followed by another directional case at 45kHz in Fig. 7(e). These results confirm the tenfold symmetrical wave beaming occurring at the identified anisotropic bands, also evidencing the twisting in the orientation of the wave directionality for different frequencies. Similarly, wave directionality results for the eightfold metamaterial plate are presented in Fig. 8. From 15 kHz to 35 kHz [Figs. 8(a)–8(d)], the reciprocal spaces show eight Fourier peaks; however, the resulting directional behavior is not as strong as the tenfold case, with the strongest directionality manifesting at a higher frequency of 45 kHz. The video animation of the time response simulation at 45 kHz is provided in the Supplemental Material (SM) [57].

The numerically predicted tenfold wave beaming around 30 kHz [Fig. 7(c)] is also experimentally confirmed in Fig. 9. Despite a shift in frequency, a good agreement is observed between numerical and experimental wave-field results at the different time snapshots of Figs. 9(a,b) and Figs. 9(d,e). Both dynamic responses exhibit directionality along tenfold symmetric directions, in agreement with the group velocity pattern depicted in Fig. 7(c). Finally, good agreement is also observed

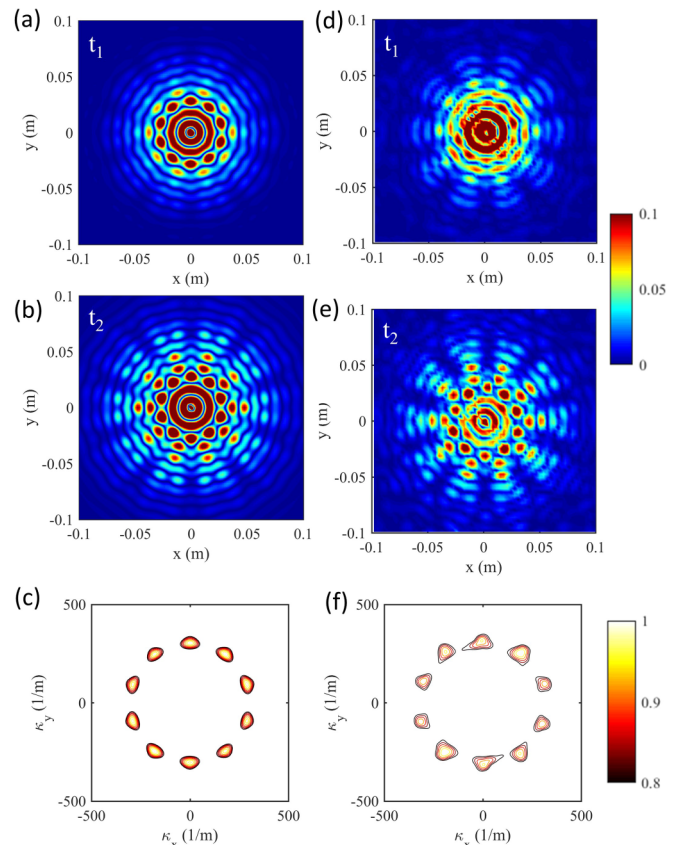


FIG. 9. Wave beaming for the tenfold quasicrystalline plate: Numerical simulation at 30 kHz (a)–(c) and experimental observation at 24.8 kHz (d)–(f), snapshot of the time response at t_1 (a), (d) and at t_2 (b), (e) with $t_2 > t_1$. And RMS of the wave-number contours averaging across all frequencies: Numerical (c) and experimental (f). A good agreement between simulation and experiment is achieved in the snapshots of the time response and in the RMS wave number contours.

between the numerical Fig. 10(c) and experimental Fig. 10(f) RMS wave number contours obtained from the 3D-FT. The video animations of the time responses for the simulation at 30 kHz and experiment at 24.8 kHz are provided in the SM [57].

V. WAVE DIFFRACTION

In this section, the directionality associated with the higher order symmetries is further exploited in the context of wave diffraction through numerical simulations. Diffraction occurs when a wave passes through an aperture or an obstacle, and has been largely employed in focusing, lensing, and antennas [58]. The combination of different apertures, i.e., metagratings, has been used to create specific wave fronts with required orientations [59]. However, wave branches with angles larger than 45° in relation to the incident wave are usually difficult to be created. Diffraction in quasicrystalline configurations, for instance, can open possibilities for superior directivity control in multiple angles as well as for loudspeakers with high quality perception [60]. In the following explorations, we focus on the tenfold symmetric plate whose directional behavior is

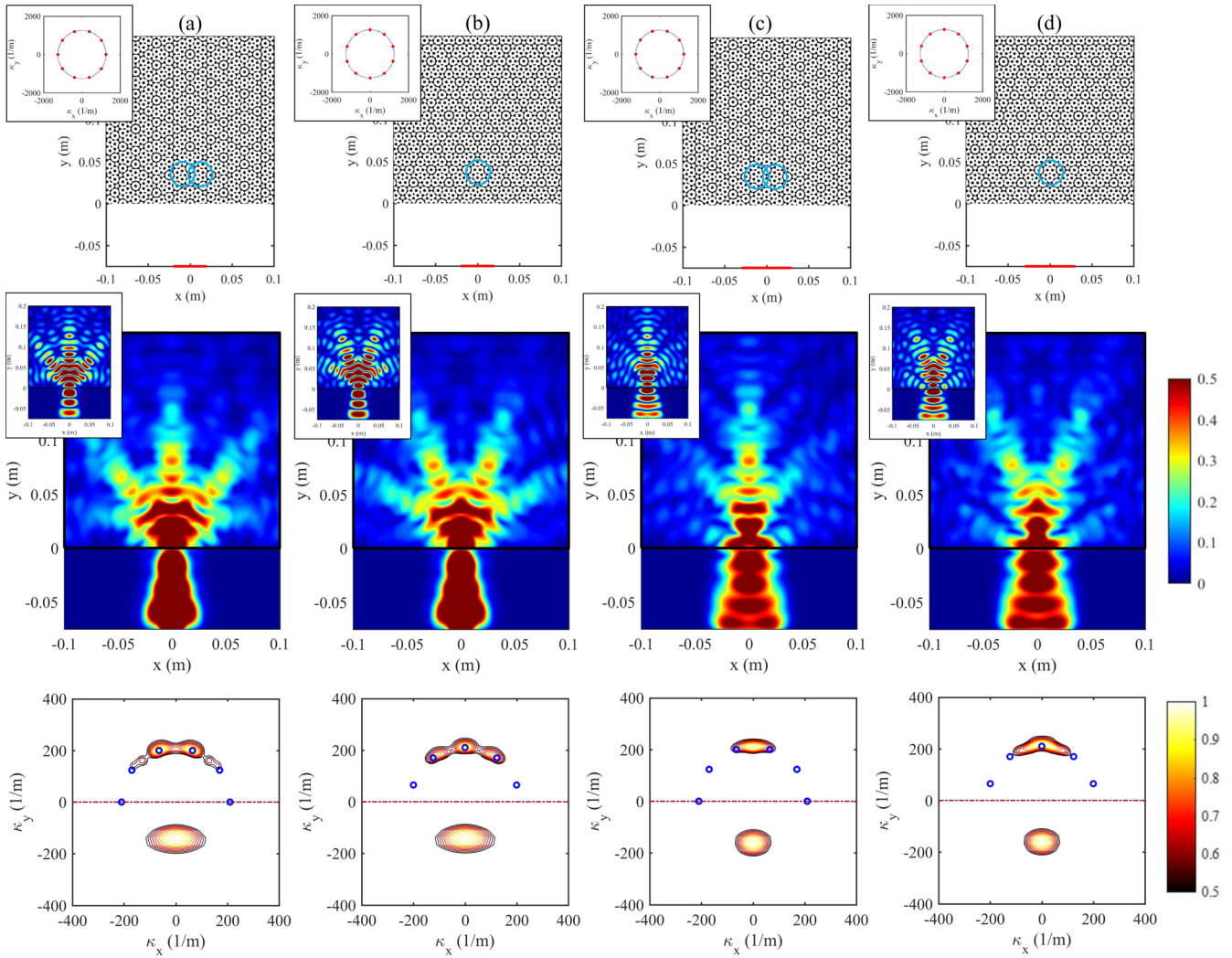


FIG. 10. Wave diffraction at 9.3 kHz in the tenfold quasiperiodic metamaterial plate. The first row shows the different scenarios where a plane wave is excited (red line) with width $b_s = 0.02$ m (a), (b) or $b_s = 0.06$ m (c), (d) in the lower homogeneous portion, and aligned (a), (c) or twisted by $\theta = \theta_N/2$ (b), (d) in relation to one of the Bragg peaks in reciprocal space at 9.3 kHz (insets). The panels in the second row depicts the RMS of the displacement field averaged across all time, with the inset representing a snapshot of the time response. The third row depicts the RMS of the wave-number contour averaged across all frequencies: $\kappa_y > 0$ for the quasicrystal plate and $\kappa_y < 0$ for the uniform plate. The blue circles correspond to the spectral peaks in the dispersion of the tenfold plate at 9.3 kHz, see Fig. 7(a). Diffraction patterns with focusing from one to four branches have been created.

stronger when compared to the eightfold plate, as highlighted in the previous section.

To illustrate the diffraction behavior, the upper half of the quasicrystal domain considered in the previous section (tenfold, $x = [-0.1, 0.1]$ m and $y = [0, 0.2]$ m) is combined to a uniform plate ($x = [-0.1, 0.1]$ m and $y = [-0.075, 0]$ m) with constant thickness $h_U = 4$ mm. Low reflection conditions are imposed at the plate boundaries to minimize backscattering. A line-source excitation is centered at the bottom of the uniform plate ($x = 0$ and $y = -0.075$ m), so the incident wave propagates along the positive y direction until it reaches the interface with the quasicrystalline domain ($y = 0$). The diffraction is illustrated by employing a sinusoidal burst excitation signal with 15 cycles for a center frequency of 9.3 kHz, corresponding to the first strong beaming behavior reported in Fig. 7.

The numerical results are summarized in Fig. 10 for different conditions that showcase different possible scenarios illustrated in the top row; the middle row displays the RMS of the wave field (a snapshot for each case is provided in the correspondent inset), while the bottom row displays the RMS of the reciprocal space content (the upper half, $\kappa_y > 0$, corresponding to the waves propagating in the quasicrystal, and the bottom half, $\kappa_y < 0$, corresponding to the incident wave in the homogeneous plate). The results in Figs. 10(a) and 10(b) correspond to a narrow line source of width 20 mm, which provides a broad wave-number content for κ_x for the incident wave, while in Figs. 10(c) and 10(d), a wider line source of 60 mm produces an incident wave with narrower wave number content for κ_x . Also, in Figs. 10(a) and 10(c), the quasicrystalline plate is designed with the conventional procedure described in Sec. II, while in Figs. 10(b) and 10(d)

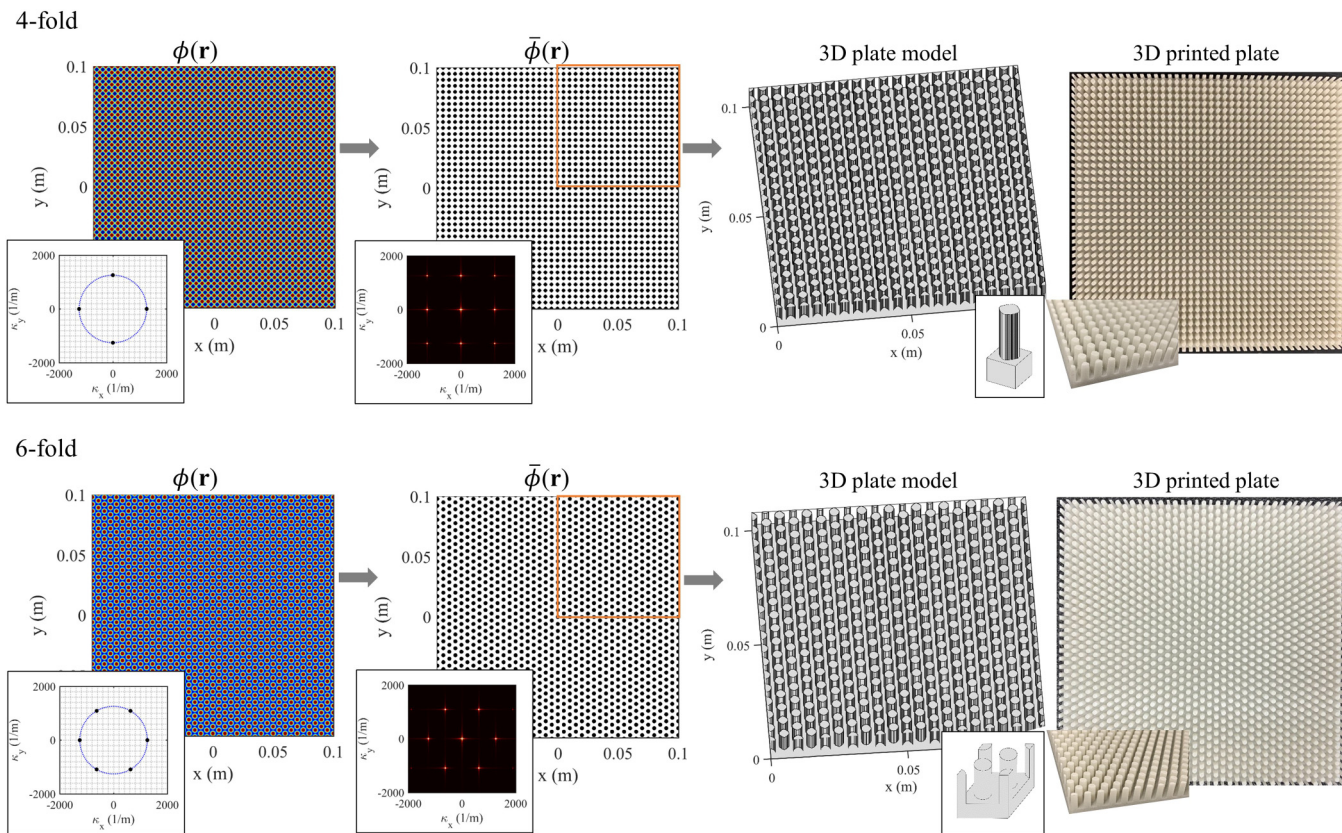


FIG. 11. Design strategy for the four- (top) and sixfold (bottom) elastic metamaterial plate with $vf = 0.30$: Two-dimensional physical distribution ϕ by assigning four or six Bragg peaks, two-phase distribution $\bar{\phi}$ after applying the threshold procedure and its Fourier transform: Phase A (white) and phase B (black). The three-dimensional plates are constructed by extruding phase B toward z direction, which produces the modulated thickness (pillars) and the correspondent 3D printed plates.

the design peaks, and the plate symmetry, are twisted by $\theta_N/2 = 18^\circ$ as depicted in the inserts of the first row. These different conditions are selected to illustrate a wealth of possibilities for wave diffraction that result in different numbers and orientations of directional branches propagating in the quasicrystalline plate.

The results are interpreted based on the intersection of the wave-number content of the incident wave (bottom half of FT panels) and the symmetry peaks of the dispersion at the excitation frequency (blue dots in upper half of the FT panels). In Fig. 10(a), the wave-number content of the incident wave reaches a zone between two Bragg peaks, which are mainly excited as evidenced by the 2D FTs. Three directional branches are observed to propagate in the plate and their directions are in agreement with the group velocity plots of Fig. 7(a). For the same plate with narrower wave number content of the incident wave Fig. 10(c), only the central region between the same peaks gets excited, resulting in a single branch propagating into the quasicrystalline portion. When the plate is twisted Figs. 10(b) and 10(d), the high symmetry points of the dispersion (blue circles) and the associated directional branches also get twisted. The broader excitation in reciprocal space produces four propagating branches Fig. 10(b), while the narrower excitation produces only 2 Fig. 10(d), and their directions are accordingly twisted by $\theta_N/2 = 18^\circ$ with respect to those in the group velocity plot

of Fig. 7(a). The video animations of the time response simulations for the different wave diffraction cases are provided in the SM [57]. These results highlight how multiple scenarios for wave diffraction can be envisioned by controlling the quasicrystal orientation and the source width, which can shift the wave behavior from beaming (i.e., multifocal) to focusing (i.e., unifocal).

VI. CONCLUSIONS

The spatial design of phononic crystals and acoustic-elastic metamaterials is based on translational periodicity, and hence, their wave phenomena, such as the directionality, are restricted to the crystallographic symmetries (e.g., two-, four- and sixfold). In this paper, the wave beaming and diffraction were expanded to high-order rotational symmetries, such as eight- and tenfold, by employing quasiperiodic elastic metamaterial plates. Their spectral contents were numerically and experimentally investigated using an approximate dispersion surface obtained from the time response and its Fourier transform. In particular, for the tenfold plate, the wave behavior becomes highly anisotropic in some frequency zones and, therefore, high-order wave directionality was observed on the dynamic response, e.g., beaming (numerically and experimentally) and diffraction (numerically). The experimental observations facilitate the implementation of quasicrystalline

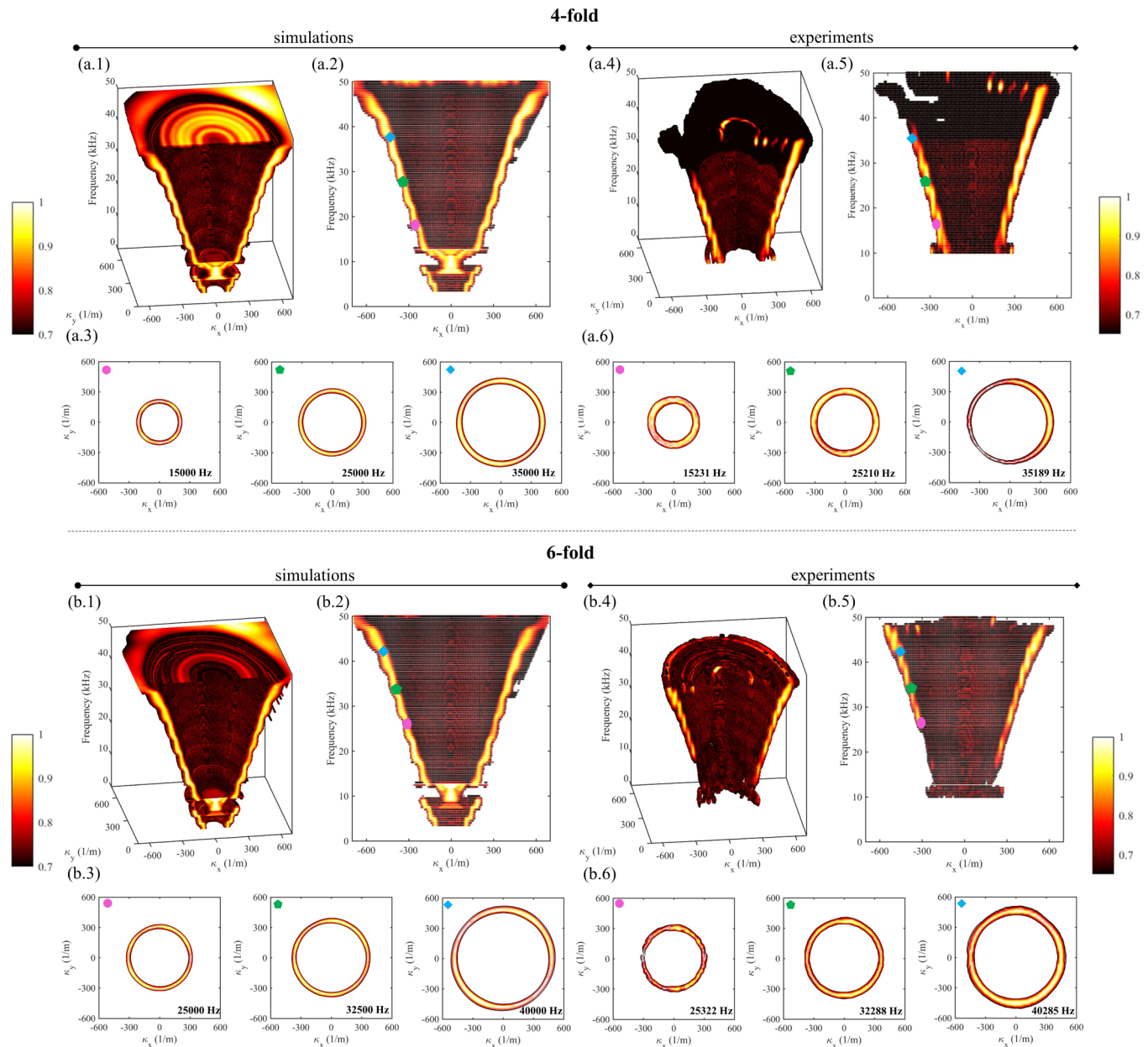


FIG. 12. Dispersion properties and contours at specific frequencies of the four- (a) and sixfold (b) elastic plate obtained by numerical simulations and experiments. Numerical and experimental results (3D spectrum and wave number contours) are in good agreement.

configurations in wave devices and structural components. Moreover, it opens possibilities for applications involving the unusual wave front directivity with high-order symmetry (e.g. eightfold, tenfold, and so on), such as focusing, sensing, and imaging beyond the symmetries provided by the periodic configurations.

ACKNOWLEDGMENTS

D.B. and C.D.M.Jr. gratefully acknowledge the support from São Paulo Research Foundation (FAPESP) through Grant References No. 2018/18774-6, No. 2019/22464-5, and No. 2018/15894-0 (research project Periodic Structure Design and Optimization for Enhanced Vibroacoustic Performance: ENVIBRO). M.I.N.R. and M.R. gratefully ac-

knowledge the support from the National Science Foundation (NSF) through Grant. No. EFRI 1741685 and from the Army Research Office through Grant No. W911NF-18-1-0036.

APPENDIX: EXTRA RESULTS FOR THE PERIODIC (crystalline) PLATES

The design strategy to conceive the four- and sixfold elastic metamaterial plates by assigning the respective number of Bragg peaks in reciprocal space is illustrated in Fig. 11. The geometric (L , λ_0 , h_A , and h_B) and material (ρ_n , E_n , ν_n , and η_n) properties as well as the volume fraction ($vf = 0.30$) are the same used in the eight- and tenfold quasicrystalline metamaterial plate presented in Sec. II. The 3D square and hexagonal unit cells are also depicted with the respective

3D elastic plate models. Their numerical and experimental approximate dispersion surfaces are shown in Fig. 12, where

almost omnidirectional wave number contours are observed for the complete frequency spectrum.

-
- [1] J. D. Joannopoulos, P. R. Villeneuve, and S. Fan, Photonic crystals: Putting a new twist on light, *Nature (London)* **386**, 143 (1997).
- [2] M. I. Hussein, M. J. Leamy, and M. Ruzzene, Dynamics of phononic materials and structures: Historical origins, recent progress, and future outlook, *Appl. Mech. Rev.* **66**, 040802 (2014).
- [3] J. Christensen, M. Kadic, O. Kraft, and M. Wegener, Vibrant times for mechanical metamaterials, *MRS Commun.* **5**, 453 (2015).
- [4] G. Ma and P. Sheng, Acoustic metamaterials: From local resonances to broad horizons, *Sci. Adv.* **2**, e1501595 (2016).
- [5] S. A. Cummer, J. Christensen, and A. Alù, Controlling sound with acoustic metamaterials, *Nat. Rev. Mater.* **1**, 13 (2016).
- [6] B. Assouar, B. Liang, Y. Wu, Y. Li, J.-C. Cheng, and Y. Jing, Controlling sound with acoustic metamaterials, *Nat. Rev. Mater.* **3**, 460 (2018).
- [7] Z. Yang, F. Gao, X. Shi, X. Lin, Z. Gao, Y. Chong, and B. Zhang, Topological Acoustics, *Phys. Rev. Lett.* **114**, 114301 (2015).
- [8] M. A. Bandres, M. C. Rechtsman, and M. Segev, Topological Photonic Quasicrystals: Fractal Topological Spectrum and Protected Transport, *Phys. Rev. X* **6**, 011016 (2016).
- [9] M. Fremling, M. van Hooff, C. Morais Smith, and L. Fritz, Existence of robust edge currents in Sierpiński fractals, *Phys. Rev. Res.* **2**, 013044 (2020).
- [10] P. Celli, B. Yousefzadeh, C. Daraio, and S. Gonella, Bandgap widening by disorder in rainbow metamaterials, *Appl. Phys. Lett.* **114**, 091903 (2019).
- [11] D. Beli, A. T. Fabro, M. Ruzzene, and J. R. F. Arruda, Wave attenuation and trapping in 3D printed cantilever-in-mass metamaterials with spatially correlated variability, *Sci. Rep.* **9**, 5617 (2019).
- [12] Y. E. Kraus and O. Zilberberg, Quasiperiodicity and topology transcend dimensions, *Nat. Phys.* **12**, 624 (2016).
- [13] Z. V. Vardeny, A. Nahata, and A. Agrawal, Optics of photonic quasicrystals, *Nat. Photonics* **7**, 177 (2013).
- [14] D. Shechtman, I. Blech, D. Gratias, and J. W. Cahn, Metallic Phase With Long-Range Orientational Order and No Translational Symmetry, *Phys. Rev. Lett.* **53**, 1951 (1984).
- [15] D. Levine and P. J. Steinhardt, Quasicrystals: A New Class of Ordered Structures, *Phys. Rev. Lett.* **53**, 2477 (1984).
- [16] M. Notomi, H. Suzuki, T. Tamamura, and K. Edagawa, Lasing Action Due to the Two-Dimensional Quasiperiodicity of Photonic Quasicrystals with a Penrose Lattice, *Phys. Rev. Lett.* **92**, 123906 (2004).
- [17] D. Luo, Q. G. Du, H. T. Dai, H. V. Demir, H. Z. Yang, W. Ji, and X. W. Sun, Strongly linearly polarized low threshold lasing of all organic photonic quasicrystals, *Sci. Rep.* **2**, 627 (2012).
- [18] J. Han, J. Xie, E. Liu, and J. Liu, Super-resolution imaging in multi-broadband of a ten-fold Penrose-type phononic quasicrystal flat lens, *Results Phys.* **19**, 103418 (2020).
- [19] Y. An, Z. Gao, and Z. Ouyang, Surface wave photonic quasicrystal, *Appl. Phys. Lett.* **116**, 151104 (2020).
- [20] S. Sakai and R. Arita, Exotic pairing state in quasicrystalline superconductors under a magnetic field, *Phys. Rev. Res.* **1**, 022002(R) (2019).
- [21] D. J. Apigo, W. Cheng, K. F. Dobiszewski, E. Prodan, and C. Prodan, Observation of Topological Edge Modes in a Quasiperiodic Acoustic Waveguide, *Phys. Rev. Lett.* **122**, 095501 (2019).
- [22] X. Ni, K. Chen, M. Weiner, D. J. Apigo, C. Prodan, A. Alù, E. Prodan, and A. B. Khanikaev, Observation of Hofstadter butterfly and topological edge states in reconfigurable quasi-periodic acoustic crystals, *Commun. Phys.* **2**, 1 (2019).
- [23] Y. Wang and O. Sigmund, Quasiperiodic mechanical metamaterials with extreme isotropic stiffness, *Extreme Mech. Lett.* **34**, 100596 (2020).
- [24] Y. Chen, M. Kadic, S. Guenneau, and M. Wegener, Isotropic chiral acoustic phonons in 3d quasicrystalline metamaterials, *Phys. Rev. Lett.* **124**, 235502 (2020).
- [25] D. Beli Jr., M. I. N. Rosa, C. D. Marqui, and M. Ruzzene, Mechanics and Dynamics of Two-Dimensional Quasicrystalline Composites, *Extreme Mech. Lett.* **44**, 101220 (2021).
- [26] Y. Chen, T. Frenzel, Q. Zhang, M. Kadic, and M. Wegener, Cubic metamaterial crystal supporting broadband isotropic chiral phonons, *Phys. Rev. Mater.* **5**, 025201 (2021).
- [27] M. Florescu, S. Torquato, and P. J. Steinhardt, Complete band gaps in two-dimensional photonic quasicrystals, *Phys. Rev. B* **80**, 155112 (2009).
- [28] M. A. Kaliteevski, S. Brand, R. A. Abram, T. F. Krauss, R. D. Rue, and P. Millar, Two-dimensional Penrose-tiled photonic quasicrystals: From diffraction pattern to band structure, *Nanotechnology* **11**, 274 (2000).
- [29] E. Rotenberg, W. Theis, K. Horn, and P. Gille, Quasicrystalline valence bands in decagonal alnico, *Nature (London)* **406**, 602 (2000).
- [30] J.-M. Gambaudo and P. Vignolo, Brillouin zone labelling for quasicrystals, *New J. Phys.* **16**, 043013 (2014).
- [31] J.-N. Fuchs, R. Mosseri, and J. Vidal, Landau levels in quasicrystals, *Phys. Rev. B* **98**, 165427 (2018).
- [32] S. S. M. Cheng, L.-M. Li, C. T. Chan, and Z. Q. Zhang, Defect and transmission properties of two-dimensional quasiperiodic photonic band-gap systems, *Phys. Rev. B* **59**, 4091 (1999).
- [33] Y. Wang, J. Liu, B. Zhang, S. Feng, and Z.-Y. Li, Simulations of defect-free coupled-resonator optical waveguides constructed in 12-fold quasiperiodic photonic crystals, *Phys. Rev. B* **73**, 155107 (2006).
- [34] A. D. Sinelnik, I. I. Shishkin, X. Yu, K. B. Samusev, P. A. Belov, M. F. Limonov, P. Ginzburg, and M. V. Rybin, Experimental observation of intrinsic light localization in photonic icosahedral quasicrystals, *Adv. Opt. Mater.* **8**, 2001170 (2020).
- [35] J.-N. Fuchs and J. Vidal, Hofstadter butterfly of a quasicrystal, *Phys. Rev. B* **94**, 205437 (2016).
- [36] R. Chen, C.-Z. Chen, J.-H. Gao, B. Zhou, and D.-H. Xu, Higher-Order Topological Insulators in Quasicrystals, *Phys. Rev. Lett.* **124**, 036803 (2020).
- [37] M. I. N. Rosa, R. K. Pal, J. R. F. Arruda, and M. Ruzzene, Edge States and Topological Pumping in Spatially

- Modulated Elastic Lattices, *Phys. Rev. Lett.* **123**, 034301 (2019).
- [38] W. Cheng, E. Prodan, and C. Prodan, Experimental Demonstration of Dynamic Topological Pumping Across Incommensurate Bilayered Acoustic Metamaterials, *Phys. Rev. Lett.* **125**, 224301 (2020).
- [39] Y. Xia, E. Riva, M. I. N. Rosa, G. Cazzulani, A. Erturk, F. Braghin, and M. Ruzzene, Experimental Observation of Temporal Pumping in Electromechanical Waveguides, *Phys. Rev. Lett.* **126**, 095501 (2021).
- [40] D. J. Apigo, K. Qian, C. Prodan, and E. Prodan, Topological edge modes by smart patterning, *Phys. Rev. Mater.* **2**, 124203 (2018).
- [41] D. Zhou, L. Zhang, and X. Mao, Topological Boundary Floppy Modes in Quasicrystals, *Phys. Rev. X* **9**, 021054 (2019).
- [42] M. I. Rosa, Y. Guo, and M. Ruzzene, Exploring topology of 1D quasiperiodic metastructures through modulated LEGO resonators, *Appl. Phys. Lett.* **118**, 131901 (2021).
- [43] M. Martí-Sabaté and D. Torrent, Dipolar localization of waves in twisted phononic crystal plates, *Phys. Rev. Appl.* **15**, L011001 (2021).
- [44] S. Spurrier and N. R. Cooper, Kane-mele with a twist: Quasicrystalline higher-order topological insulators with fractional mass kinks, *Phys. Rev. Res.* **2**, 033071 (2020).
- [45] M. I. Rosa, M. Ruzzene, and E. Prodan, Topological gaps by twisting, *Commun. Phys.* **4**, 1 (2021).
- [46] M. Koshino and H. Oka, Topological invariants in two-dimensional quasicrystals, *Phys. Rev. Res.* **4**, 013028 (2022).
- [47] M. Ruzzene, F. Scarpa, and F. Soranna, Wave beaming effects in two-dimensional cellular structures, *Smart Mater. Struct.* **12**, 363 (2003).
- [48] M. Ruzzene and F. Scarpa, Directional and band-gap behavior of periodic auxetic lattices, *Phys. Status Solidi B* **242**, 665 (2005).
- [49] A. S. Phani, J. Woodhouse, and N. A. Fleck, Wave propagation in two-dimensional periodic lattices, *J. Acoust. Soc. Am.* **119**, 1995 (2006).
- [50] S. Gonella and M. Ruzzene, Analysis of in-plane wave propagation in hexagonal and re-entrant lattices, *J. Sound Vib.* **312**, 125 (2008).
- [51] G. Trainiti, J. Rimoli, and M. Ruzzene, Wave propagation in undulated structural lattices, *Int. J. Solids Struct.* **97-98**, 431 (2016).
- [52] D. Beli, J. Arruda, and M. Ruzzene, Wave propagation in elastic metamaterial beams and plates with interconnected resonators, *Int. J. Solids Struct.* **139-140**, 105 (2018).
- [53] A. Foehr, O. R. Bilal, S. D. Huber, and C. Daraio, Spiral-Based Phononic Plates: From Wave Beaming to Topological Insulators, *Phys. Rev. Lett.* **120**, 205501 (2018).
- [54] T. Lubensky, Symmetry, elasticity, and hydrodynamics in quasiperiodic structures, in *Introduction to Quasicrystals, Aperiodicity and Order*, Vol. 1, edited by M. V. Jarić (Elsevier, 1988), Chap 6, pp. 199–280.
- [55] M. Widom, Discussion of phasons in quasicrystals and their dynamics, *Philos. Mag.* **88**, 2339 (2008).
- [56] D. R. Hofstadter, Energy levels and wave functions of Bloch electrons in rational and irrational magnetic fields, *Phys. Rev. B* **14**, 2239 (1976).
- [57] See Supplemental Material at <https://link.aps.org/supplemental/10.1103/PhysRevResearch.4.043030> for the wave beaming and diffraction video animations.
- [58] Y. Ra'adi, D. L. Sounas, and A. Alù, Metagratings: Beyond the Limits of Graded Metasurfaces for Wave Front Control, *Phys. Rev. Lett.* **119**, 067404 (2017).
- [59] V. Popov, F. Boust, and S. N. Burokur, Controlling Diffraction Patterns with Metagratings, *Phys. Rev. Appl.* **10**, 011002(R) (2018).
- [60] A. M. Pasqual, P. Herzog, and J. R. d. F. Arruda, Theoretical and experimental analysis of the electromechanical behavior of a compact spherical loudspeaker array for directivity control, *J. Acoust. Soc. Am.* **128**, 3478 (2010).